Food Frontiers

WILEY

RESEARCH ARTICLE OPEN ACCESS

pH-Shift-Prepared *Chlorella pyrenoidosa* Protein/Peptide–Calcium Complexes Improve Skeletal Health by Enhanced Intestinal Calcium Utilization in Calcium-Deficient Rats

Yan Yang[1,2] | Shenwan Wang[1,2] | Qimeng Zhou[1,2] | Ye Qi[1,2] | Bin Zhou[3] | Jing Li[1,2] | Tao Hou[1,2] | Bin Li[1,2] | Hongshan Liang[1,2]

[1]College of Food Science and Technology, Huazhong Agricultural University, Wuhan, China | [2]Key Laboratory of Environment Correlative Dietology (Huazhong Agricultural University), Ministry of Education, Wuhan, China | [3]School of Biological Engineering and Food, Hubei University of Technology, Wuhan, China

Correspondence: Hongshan Liang (lianghongshan@mail.hzau.edu.cn)

Received: 3 January 2026 | **Revised:** 10 March 2026 | **Accepted:** 18 March 2026

Keywords: bone health | calcium utilization | *Chlorella pyrenoidosa* | peptide–calcium chelate | pH-shift

ABSTRACT

Calcium carbonate supplements often exhibit limited solubility and gastrointestinal precipitation, restricting calcium availability. To address this limitation, an enzyme-free pH-shift strategy was applied to prepare *Chlorella pyrenoidosa* protein (CPP)/peptide–calcium complexes (pH–Ca) and to evaluate their effects on calcium utilization in calcium-deficient rats. Alkaline pH-shift treatment promoted protein unfolding and increased the accessibility of calcium-binding groups, resulting in an effective chelation rate of 44.04% ± 1.34% under optimized conditions (pH 13, 4 h). Spectroscopic analyses indicated the formation of predominantly amorphous protein/peptide–calcium complexes. In vivo, pH–Ca supplementation significantly improved bone mineral indices, microarchitecture, and mechanical strength compared with calcium carbonate and untreated protein–calcium controls. These skeletal benefits were accompanied by partial restoration of duodenal morphology, normalization of intestinal calcium transport–related gene expression, and increased gut microbiota diversity. Overall, pH-shift-prepared CPP/peptide–calcium complexes enhance intestinal calcium utilization and skeletal outcomes in calcium-deficient rats.

Abbreviations: AAR, apparent calcium absorption; ACE, abundance-based coverage estimator; ALP, alkaline phosphatase; AMP, amplicon sequence variant; ANOVA, analysis of variance; BMD, bone mineral density; BV/TV, bone volume fraction; Ca, calcium; CaBP-D9k, calbindin-D9k; $CaCO_3$, calcium carbonate; CPP, *Chlorella pyrenoidosa* protein; CPPs, *Chlorella pyrenoidosa* peptides; Ct.Ar, cortical bone area; Ct.Th, cortical bone thickness; CTX-I, C-terminal telopeptide of type I collagen; DAB, 3,3′-diaminobenzidine; DW, dry weight; EDTA, ethylenediaminetetraacetic acid; ELISA, enzyme-linked immunosorbent assay; FTIR, Fourier transform infrared; GH, growth hormone; H&E, hematoxylin and eosin; HRP, horseradish peroxidase; IGF-1, insulin-like growth factor 1; IL-17, interleukin-17; IL-6, interleukin-6; micro-CT, micro-computed tomography; NC, normal control; OCN, osteocalcin; OPLS-DA, orthogonal partial least squares-discriminant analysis; OTU, operational taxonomic unit; PDI, polydispersity index; PINP, N-terminal propeptide of type I procollagen; PMCA1b, plasma membrane Ca^{2+}-ATPase 1b; PTH, parathyroid hormone; qPCR, quantitative real-time polymerase chain reaction; SH, sulfhydryl; Tb.N, trabecular number; Tb.Pf, trabecular pattern factor; Tb.Sp, trabecular separation; Tb.Th, trabecular thickness; TNF-α, tumor necrosis factor-α; TRAP, tartrate-resistant acid phosphatase; TRAP-5b, tartrate-resistant acid phosphatase 5b; *TRPV6*, transient receptor potential vanilloid 6; UV–Vis, ultraviolet–visible; XRD, x-ray diffraction.

Yan Yang and Shenwan Wang should be considered joint first authors.

This is an open access article under the terms of the Creative Commons Attribution License, which permits use, distribution and reproduction in any medium, provided the original work is properly cited.

© 2026 The Author(s). *Food Frontiers* published by John Wiley & Sons Australia, Ltd and Nanchang University, Northwest University, Jiangsu University, Zhejiang University, Fujian Agriculture and Forestry University.

1 | Introduction

Calcium (Ca) is an essential nutrient required for maintaining critical physiological functions, including bone mineralization, nerve conduction, and muscle contraction. Ca deficiency is particularly critical during the growth and development period. During this time, children's bodies not only undergo rapid growth but also experience significant changes in areas such as the brain, bones, and immune system. Notably, elevated inflammatory cytokines (such as interleukin-6 (IL-6) and tumor necrosis factor-α [TNF-α] in chronic inflammatory diseases (e.g., inflammatory bowel disease) can lead to growth retardation by inhibiting the growth hormone (GH)/IGF-I axis signaling pathway, and this exhibits a synergistic effect with the negative impact of Ca deficiency on bone growth (Pass et al. 2009). Bone development requires sufficient mineral support, including Ca, magnesium, and zinc, to ensure bone density and strength. Inadequate dietary Ca intake will impact children's development, affecting children's growth and overall health (Z. Wang et al. 2025). Current commercial Ca supplements, such as Ca carbonate, exhibit several drawbacks, including low bioavailability, considerable gastrointestinal irritation, and vulnerability to dietary components. These limitations render them inefficient for optimal Ca supplementation (J. Chen et al. 2017). Protein/peptide–Ca complexes have attracted attention as food-derived Ca carriers because coordination with peptides can maintain Ca in a soluble form and facilitate intestinal uptake through peptide-associated transport pathways (Lin et al. 2024). Previous studies suggest that Ca bioavailability from peptide-based systems depends not only on chemical coordination but also on physicochemical features such as molecular conformation, surface charge, and colloidal stability under gastrointestinal conditions (Qu et al. 2022). These properties collectively influence dispersion behavior, resistance to precipitation, and interaction with the intestinal epithelium.

Microalgal proteins represent a sustainable and nutritionally valuable source for functional food applications. *Chlorella pyrenoidosa* is particularly rich in acidic amino acids, including aspartic acid (Asp) and glutamic acid (Glu), whose carboxyl groups are effective Ca-coordination sites (Bu et al. 2024; Ursu et al. 2014). However, native algal proteins often adopt compact conformations that limit the accessibility of these functional groups (Y. Chen et al. 2019; Li et al. 2020). Conventional preparation of protein/peptide–Ca complexes typically relies on enzymatic hydrolysis followed by fractionation and chelation. Such multistep processes are associated with high enzyme costs, batch-to-batch variability, and challenges in industrial scale-up (Erdem and Woodley 2024; M. Liu et al. 2025). Consequently, there is a pressing need to develop an enzyme-free, clean-label, and low-cost preparation technology that enhances the Ca utilization efficiency of the resulting products.

The pH-shift method facilitates protein conformational unfolding and selective peptide bond cleavage by temporarily adjusting the pH of system. This process enriches the protein with short peptides that contain Ca-binding sites (Long et al. 2025; Sultan et al. 2024). Under acidic conditions, protein conformations unfold, and Asp-Pro and similar peptide bonds are preferentially cleaved, exposing additional Asp/Glu residues. In alkaline conditions, the carboxyl groups of amino acid side chains deprotonate, which increases the negative charge density and strengthens the electrostatic interaction with Ca ions (Mollaev et al. 2021; T. Zhang et al. 2024). Unlike enzymatic hydrolysis, this method does not require the addition of exogenous enzymes, offering a simpler process at a lower cost. By adjusting the pH, it enables precise optimization of the exposure efficiency of Ca-binding sites, providing a promising technical foundation for enhancing the Ca utilization performance of peptide–Ca chelates (Jiang et al. 2011).

Despite these potential advantages, the role of pH-shift-derived protein/peptide–Ca complexes in promoting intestinal Ca utilization and skeletal outcomes remains insufficiently understood. In particular, how such systems influence intestinal morphology, Ca transport-related gene expression, and downstream bone metabolism has not been systematically investigated. Addressing these questions is crucial for clarifying the functional relevance of Ca delivery systems derived from food proteins and produced via the pH-shift method.

In this context, the present study employed an enzyme-free pH-shift strategy to prepare Ca-coordinated complexes from *C. pyrenoidosa* proteins (CPP). The work aimed to elucidate how pH-induced structural modification of protein/peptide systems relates to Ca utilization at the intestinal level and subsequent skeletal responses in a Ca-deficient rat model. For clarity, the term "protein/peptide–Ca complexes" in this study refers to Ca-coordinated systems derived from pH-shift-treated Chlorella proteins, comprising unfolded protein fragments and peptide segments rather than extensively hydrolyzed peptides.

2 | Materials and Methods

2.1 | Materials and Reagents

CPP powder (protein content ≥90%) was provided by Shaanxi Baichuan Biotechnology Co. Ltd. (Shanxi, China). Calcium chloride ($CaCl_2$), calcium carbonate ($CaCO_3$), sodium hydroxide (NaOH), hydrochloric acid (HCl), and absolute ethanol were purchased from Sinopharm Chemical Reagent Co. Ltd. (Shanghai, China). Commercial assay kits for free sulfhydryl groups, serum biochemical indices, and enzyme-linked immunosorbent assay (ELISA) were obtained from Solarbio Science and Technology Co. Ltd. (Beijing, China) and Nanjing Jiancheng Bioengineering Institute (Nanjing, China). All reagents were of analytical grade unless otherwise specified.

2.2 | Preparation of pH-Shift-Prepared Protein/Peptide–Ca Complexes

CPP was dispersed in deionized water (100 mg/mL) and subjected to pH-shift treatment to induce protein unfolding and partial peptide generation. The suspension pH was adjusted to 2, 4, 6, 7, 9, or 13 using 6 M HCl or 6 M NaOH, followed by continuous stirring (300 rpm) at ambient temperature for 1–5 h. After treatment, samples were centrifuged at 10,000 rpm for 10 min at 4°C. The supernatants were collected, neutralized to pH 7.0, and lyophilized to obtain pH-treated protein/peptide fractions (pH-

pro). Untreated protein suspension (pH ≈ 6.0) was used as the native control.

For Ca coordination, $CaCl_2$ was added to the pH-pro solution at a protein-to-$CaCl_2$ mass ratio of 10:1. The mixture was incubated at 37°C for 2 h with gentle shaking (150 rpm). After incubation, samples were centrifuged (10,000 rpm, 10 min), and the supernatant was collected. Unchelated Ca was removed by ethanol precipitation (nine volumes of absolute ethanol). The precipitates were collected, washed, and lyophilized to obtain pH-shift-prepared protein/peptide–Ca complexes (pH–Ca).

Ca chelation rate (%) was determined by atomic absorption spectrophotometry (AA-6300C, Shimadzu, Japan) at 422.7 nm using a standard Ca curve. Chelation rate (%) was calculated as

$$\text{Chelation rate}\,(\%) = \frac{C_1 V_1 X_1}{C_2 V_2 X_2} \times 100 \quad (1)$$

where C_1 is Ca concentration in the chelate (μg/mL), V_1 is its volume (mL), X_1 is its dilution factor, C_2 is total Ca in the stock (μg/mL), V_2 is reaction volume (mL), and X_2 is the stock dilution factor.

2.3 | Characterization

2.3.1 | Determination of Free Sulfhydryl Content

Free SH content under different pH/time conditions was measured using the commercial kit with reduced glutathione as standard, following the manufacturer's protocol.

2.3.2 | Amino Acid Composition Analysis

Hydrolyzed amino acid profiles were determined using an automatic amino acid analyzer (Biochrom 30+, UK) according to GB 5009.124-2016. Samples (50 mg) were hydrolyzed with 6 M HCl under nitrogen protection at 110°C for 22–24 h. After evaporation and reconstitution in sodium citrate buffer (pH 2.2), samples were filtered and analyzed.

2.3.3 | Free Carboxyl Group Content Analysis

The carboxyl group content (Q_{COOH}, mmol/g) was determined by titration. Briefly, 0.1 g of the sample was added to 100 mL of a 0.01 mol/L NaOH aqueous solution and stirred evenly at room temperature. The residual NaOH was then titrated with 0.01 mol/L HCl to the endpoint. A reagent blank was performed in parallel and used for correction. Q_{COOH} was calculated using the following equation:

$$Q_{COOH}\,(\text{mmol/g}) = \frac{(C_1 V_1 - C_2 V_2)}{m} \quad (2)$$

where C_1(mol/L) and V_1(mL) are the concentration and volume of NaOH added, C_2(mol/L) and V_2(mL) are the concentration and volume of HCl consumed to neutralize the residual NaOH, and m(g) is the sample mass.

2.3.4 | Zeta Potential Analysis

Zeta potential of pH-pro and pH–Ca samples (1 mg/mL) was measured using a Zetasizer Nano ZS (Malvern Instruments, UK) to assess surface charge characteristics.

2.3.5 | Ultraviolet–Visible Absorption Analysis

pH-pro and pH–Ca, with the highest chelation rates, were diluted to 0.5 mg/mL. UV–Vis spectra were recorded using a UV–Vis spectrophotometer (UV-1100, Mapada Instruments, Shanghai, China) at a scan speed of 60 nm/min and bandwidth of 2.0 nm. Each spectrum was the average of three scans.

2.3.6 | Fourier Transform Infrared Spectral Analysis

Dried samples (pH-pro, pH–Ca) were mixed with KBr (1:100, w/w), ground, and pressed into pellets. Spectra were collected on a Nicolet Nexus 470 (Thermo, USA) from 400–4000 cm^{-1}, 32 scans, with KBr background subtraction ($n = 3$).

2.3.7 | X-Ray Diffraction Analysis

XRD patterns were obtained using a Bruker D8 Advance diffractometer (Bruker, Germany) to evaluate the crystalline or amorphous nature of the complexes.

2.4 | Animal Experimentation

2.4.1 | Animal Model and Experimental Design Diets

All animal experimental procedures were conducted in accordance with the ARRIVE guidelines and complied with the National Guidelines for the Care and Use of Laboratory Animals of China. The experimental protocol was approved by the Animal Ethics Committee of Huazhong Agricultural University under license SYXK (Hubei) 2020-0084, with an ethical approval number HZAURA-2025-0029. Thirty male Sprague-Dawley rats (3 weeks old, 95 ± 10 g) were obtained from a certified laboratory animal supplier. After a 1-week acclimation period, rats were randomly assigned to five groups ($n = 6$): normal control (NC), low-Ca model (Model), $CaCO_3$, native-pro-Ca, and pH–Ca groups. The NC group received a standard AIN-93G diet (0.5% Ca), whereas all other groups were fed a low-Ca diet (0.1% Ca). Ca supplements were administered by oral gavage once daily for 4 weeks at a dose equivalent to 66.67 mg Ca/kg body weight (Y. Liang et al. 2025). The detailed composition of the experimental diets is shown in Table 1. Body weight was recorded at baseline and every 2 days, and 4-week weight gain was calculated.

Due to budget constraints for some high-cost assays, only a randomly selected subset of samples from each group was used for these analyses. The exact sample size (n) for each assay is indicated in the corresponding figure/table legend. Random selection was performed without considering outcomes, and all other procedures remained unchanged.

TABLE 1 | Composition of the AIN-93G diet and the low-calcium diet used in the study.

Ingredient (g)	AIN-93G	Low calcium diet
Casein	200	200
L-cystine	3	3
Cornstarch	397.5	397.5
Maltodextrin	132	132
Sucrose	100	100
Cellulose	50	50
Soybean oil	70	70
Vitamin MixV10037	10	10
Mineral MixS10022G	35 (Calcium 5)	35 (Calcium 1)
Choline bitartrate	2.5	2.5

2.4.2 | Tissue Collection

At Week 4, rats were fasted for 12 h prior to sample collection. Under general anesthesia, blood (2 mL) was collected via orbital venous plexus puncture, allowed to clot at 4°C, and centrifuged (4000 rpm, 10 min) to obtain serum. Following blood collection, rats were humanely euthanized by cervical dislocation in accordance with institutional animal care and use guidelines. Rats were euthanized by cervical dislocation following the 3R principle. The liver, spleen, and kidneys were excised, rinsed with saline, blotted dry, and weighed. A 1 cm segment of the duodenum (2 cm distal to the pylorus) was collected, with one portion fixed in 4% paraformaldehyde and the other preserved in RNA fixative. Bilateral femurs and tibias were harvested; one side was fixed in 4% paraformaldehyde, and the contralateral side was wrapped in saline-soaked gauze and stored at −20°C for further analysis.

2.4.3 | Ca Metabolism Experiment

In the second week of the experiment, rats were transferred to metabolic cages for a 3-day Ca balance study. During this period, daily gavage was administered at fixed times. The amount of feed provided was recorded, and the uneaten feed was weighed 24 h later to calculate food intake. Feces were collected and promptly frozen, then later dried at 105°C to constant weight to record the dry weight (DW). Urine was collected quantitatively over 24 h, acidified with dilute nitric acid, and stored at −20°C until Ca determination. Ca concentrations in diet, feces, and urine were measured by atomic absorption spectrophotometry. Apparent Ca absorption rate (AAR), fecal Ca excretion, and net Ca retention were calculated. AAR was calculated using the following equation:

$$\mathrm{AAR}(\%) = (\mathrm{Ca\ intake} - \mathrm{Fecal\ Ca})/\mathrm{Ca\ intake} \times 100 \quad (3)$$

2.4.4 | Bone Measurements and Microstructural Analysis

Femur and tibia length and diameter were measured using a digital caliper. Bone DW and Ca content were determined after drying and acid digestion. Biomechanical properties were evaluated by a three-point bending test using a universal testing machine (Instron 5943, Instron Corporation, Norwood, MA, USA) (M. Zhao et al. 2022). Bone microarchitecture was assessed by micro-computed tomography (micro CT, NMC-200, Pingsheng Medical Technology (Kunshan) Co. Ltd.), and parameters, including bone volume fraction (BV/TV, %), trabecular thickness (Tb.Th, mm), trabecular separation (Tb.Sp, mm), trabecular number (Tb.N, mm^{-1}), trabecular pattern factor (Tb.Pf, mm^{-1}), bone mineral density (BMD, mg/cm^3), cortical bone thickness (Ct.Th, mm), and cortical bone area (Ct.Ar, mm^2), were calculated. For trabecular bone analysis, a cuboidal region of interest (ROI) was selected starting at a distance of 2 mm distal to the growth plate to exclude the primary spongiosa before extending 4 mm along the longitudinal axis of the femur or tibia. For cortical bone analysis, a separate ROI was selected starting at 8 mm distal to the growth plate and extending for 2 mm in length along the longitudinal axis of the femur or tibia. A nominal isotropic voxel size of 50 μm (0.05 mm) was used for scanning. The minimum achievable reconstructed pixel size of the system is 2 μm. A global thresholding method was applied to segment bone from non-bone tissue in the reconstructed 3D images.

2.4.5 | Serum Biochemistry Analysis

Serum Ca, phosphorus (P), and alkaline phosphatase (ALP) were measured per kit instructions (Nanjing Jiancheng). Parathyroid hormone (PTH), OCN, N-terminal propeptide of type I procollagen (PINP), C-terminal telopeptide of type I collagen (CTX-I), tartrate-resistant acid phosphatase 5b (TRAP-5b), TNF-α, IL-17, and IL-6 were quantified per ELISA kit manuals (Jiangsu Meimian). Detailed information for all assay kits is provided in Table S1. All ELISA kits were rat-specific. Colorimetric kits were used for rat serum samples according to the manufacturers' instructions.

2.4.6 | Assessment of Intestinal Morphology

Duodenal segments were fixed in 4% paraformaldehyde, embedded in paraffin, sectioned (4 μm), and stained with hematoxylin and eosin (H&E). Villus height, crypt depth, and goblet cell number were quantified using CaseViewer software.

2.4.7 | RNA Extraction and Quantitative Real-Time PCR (qPCR)

Total RNA was extracted from frozen duodenal samples using TRI Reagent (Beijing Lanjie Ke Technology Co. Ltd.). RNA concentration and purity were determined using an N60 Touch microvolume spectrophotometer (Beijing Implen International Trading Co. Ltd.). Total RNA was reverse-transcribed into cDNA using the TakaRa RR036A reverse transcription kit (Dalian Takara Bio Inc.). qPCR was performed on a QuantStudio 6 Flex System (Thermo Fisher Scientific Inc., USA) using SYBR Green Master Mix (Dalian Takara Bio Inc.) and gene-specific primers (1 mM; primer sequences are listed in Table S2). The PCR cycling conditions included initial denaturation at 95°C for 5 min

followed by 40 cycles of 95°C for 15 s and 60°C for 30 s annealing and extension. Relative gene expression levels were determined with the comparative C_t ($\Delta\Delta C_t$) method, with GAPDH as the reference gene.

2.4.8 | Bone Histochemical Staining and Quantification

2.4.8.1 | Osteocalcin (OCN) Immunohistochemistry. Femurs were fixed in 4% paraformaldehyde, decalcified in 10% EDTA (pH 7.4), embedded in paraffin, and sectioned. After antigen retrieval and blocking, sections were incubated overnight at 4°C with a rabbit anti-OCN antibody (1:100; Servicebio, China), followed by HRP-conjugated secondary antibody. Immunoreactivity was visualized using DAB and counterstained with hematoxylin. OCN-positive cells were observed under a light microscope (Nikon E100, Japan) and quantified using ImageJ from randomly selected metaphyseal regions.

2.4.8.2 | Tartrate-Resistant Acid Phosphatase Staining and Osteoclast Quantification. Paraffin sections were stained TRAP using a commercial kit according to the manufacturer's protocol. TRAP-positive osteoclasts were identified by red cytoplasmic staining and quantified as the number of TRAP-positive cells per bone surface area in trabecular regions using ImageJ.

2.4.9 | DNA Extraction and 16S rRNA Amplicon Sequencing Analysis

Bacterial DNA was extracted from fecal samples ($n = 5$ rats per group) using the MoBio PowerSoil DNA Isolation Kit according to the manufacturer's protocol. The V3–V4 hypervariable region of the bacterial 16S rRNA gene was amplified via PCR using the primer pair 341F (5′-CCTAYGGGRBGCASCAG-3′) and 806R (5′-GGACTACNNGGGTATCTAAT-3′). Amplified products were purified, quantified, and sequenced on the Illumina NovaSeq platform, generating 250-bp paired-end reads. Raw sequencing reads were processed using the QIIME 2 (Quantitative Insights Into Microbial Ecology 2) pipeline following the "Atacama Soil Microbiome Tutorial" workflow, supplemented with custom scripts. In brief, sequences underwent dereplication, quality filtering, and merging into high-quality consensus sequences (amplicon sequence variants). Operational taxonomic units (OTUs) were clustered at a 97% sequence similarity threshold and taxonomically classified against the SILVA reference database (version 138). Absolute bacterial abundance was estimated for each sample by normalizing total DNA yield to the average genomic DNA mass per bacterial cell, providing an approximation of microbial load.

2.5 | Statistical Analysis

Data conforming to normal distribution and homogeneity of variance were analyzed by one-way analysis of variance (ANOVA) and multiple comparisons using Tukey's honestly significant difference (HSD) test. Data are expressed as mean ± standard deviation (SD). The sample size (n) refers to the number of biological replicates for each analysis. $P < 0.05$ in the statistical results indicated that the difference was statistically significant.

3 | Results

3.1 | Effects of pH-Shift Conditions on Ca Chelation Capacity and Structural Features of CPP

As shown in Figure 1A, chelation efficiency increased progressively with increasing alkalinity and treatment duration, reaching a maximum at pH 13 after 4 h (44.04% ± 1.34%, $p < 0.05$), which was therefore selected for subsequent analyses. The calcium content of the prepared native-pro-Ca and pH–Ca was further determined, with the specific values shown in Table S3. In parallel with enhanced chelation, pH-shift treatment substantially altered protein structural exposure. Free sulfhydryl (–SH) content increased significantly under alkaline conditions, with the highest level observed at pH 13 (Figure 1B), consistent with extensive unfolding and disulfide bond disruption. Prolonged treatment beyond 4 h resulted in a slight decline in –SH content. Amino acid analysis further showed that pH-shift treatment altered the hydrolyzed amino acid profile of *Chlorella* proteins (Table 2). Although the relative contents of Asp and Glu varied across pH conditions, maximal chelation under strong alkalinity occurred despite these compositional changes. Notably, Q_{COOH} reached the highest value at pH 13 (Table 3), which is consistent with the condition showing the maximum Ca chelation rate. We have revised the discussion accordingly to clarify that increased Q_{COOH} reflects greater availability/exposure of carboxyl ligands, whereas acknowledging that Q_{COOH} is an indirect indicator rather than a direct measurement of Ca^{2+} coordination. Table 4 provides a comparative overview of the protein/peptide–Ca complexes prepared in this study and those reported previously, including differences in hydrolysis strategies, Ca-binding capacity, and available bioavailability evidence.

3.2 | Structural Features of pH-Shift-Prepared Protein/Peptide–Ca Complexes

Both pH-treated proteins (pH-pro) and protein/peptide–Ca complexes (pH–Ca) carried net negative surface charges (Figure 1C), whereas Ca coordination significantly reduced the absolute zeta potential from −8.65 to −6.65 mV ($p < 0.05$). UV–Vis spectra showed a hypsochromic shift of the maximum absorption wavelength ($\Delta\lambda_{max} = -3$ nm) after Ca binding (Figure 1D). FTIR analysis revealed distinct band shifts in the N–H/O–H stretching region and in the amide I and II regions, as well as changes in carboxylate-associated bands, indicating the involvement of amino and carboxyl functional groups in Ca coordination (Figure 1E). XRD patterns of pH–Ca exhibited broad diffraction features with altered peak positions and widths compared with pH-pro, consistent with the formation of a predominantly amorphous coordination complex (Figure 1F).

3.3 | Ca Metabolism Experiment

Figure 2A–C presents the effects of different Ca supplements on Ca intake, absorption, excretion, and retention during the

TABLE 2 | Amino acid composition of protein hydrolysates prepared at the indicated pH.

Amino acids (mg/g)	pH 2	pH 4	pH 6	pH 7	pH 9	pH 13
Asp	53.47 ± 1.20^{c}	56.66 ± 0.70^{ab}	57.09 ± 0.72^{ab}	57.62 ± 0.99^{a}	55.25 ± 0.55^{bc}	45.76 ± 0.49^{d}
Thr	14.37 ± 0.59^{b}	16.27 ± 0.53^{a}	17.24 ± 0.12^{a}	16.78 ± 0.22^{a}	16.22 ± 0.16^{a}	12.74 ± 0.37^{c}
Ser	30.78 ± 0.67^{b}	32.85 ± 0.60^{a}	33.75 ± 0.42^{a}	33.59 ± 0.33^{a}	33.35 ± 0.98^{a}	25.18 ± 0.32^{c}
Glu	101.59 ± 0.57^{d}	109.59 ± 0.28^{bc}	110.66 ± 0.69^{ab}	111.33 ± 0.22^{a}	108.34 ± 0.44^{c}	87.58 ± 0.60^{e}
Gly	145.31 ± 0.33^{c}	155.59 ± 0.61^{ab}	155.95 ± 0.06^{a}	154.91 ± 0.43^{ab}	153.89 ± 0.60^{b}	134.68 ± 1.10^{d}
Ala	78.02 ± 0.50^{d}	81.44 ± 0.63^{c}	81.79 ± 0.47^{bc}	85.76 ± 0.61^{a}	83.41 ± 0.85^{b}	68.06 ± 0.45^{e}
Cys	14.73 ± 0.31^{ab}	13.89 ± 0.25^{b}	15.19 ± 0.47^{a}	14.93 ± 0.23^{a}	15.05 ± 0.20^{a}	13.90 ± 0.42^{b}
Val	20.49 ± 0.32^{d}	21.74 ± 0.35^{ab}	22.38 ± 0.16^{a}	21.37 ± 0.36^{bc}	20.91 ± 0.31^{cd}	17.81 ± 0.19^{e}
Met	5.61 ± 0.33^{b}	5.96 ± 0.04^{ab}	6.00 ± 0.03^{ab}	5.85 ± 0.05^{ab}	6.02 ± 0.05^{a}	5.03 ± 0.01^{c}
Ile	12.73 ± 0.30^{c}	14.04 ± 0.14^{ab}	14.60 ± 0.49^{a}	14.15 ± 0.05^{ab}	13.77 ± 0.12^{b}	10.92 ± 0.12^{d}
Leu	26.15 ± 0.20^{d}	28.46 ± 0.51^{ab}	27.73 ± 0.15^{c}	28.98 ± 0.26^{a}	28.09 ± 0.09^{bc}	22.74 ± 0.20^{e}
Tyr	5.30 ± 0.07^{c}	5.10 ± 0.01^{d}	5.04 ± 0.03^{d}	6.30 ± 0.05^{a}	5.11 ± 0.04^{b}	5.44 ± 0.03^{d}
Phe	16.68 ± 0.13^{b}	18.10 ± 0.10^{a}	18.11 ± 0.03^{a}	18.13 ± 0.01^{a}	17.97 ± 0.03^{a}	15.15 ± 0.04^{c}
His	5.52 ± 0.08^{d}	5.99 ± 0.02^{b}	6.23 ± 0.04^{a}	6.00 ± 0.02^{b}	5.71 ± 0.03^{c}	5.42 ± 0.04^{d}
Lys	32.10 ± 0.05^{e}	35.01 ± 0.13^{d}	36.16 ± 0.04^{b}	37.06 ± 0.07^{a}	35.70 ± 0.03^{c}	28.75 ± 0.02^{f}
Arg	68.94 ± 0.14^{d}	73.22 ± 0.20^{c}	72.70 ± 0.40^{c}	75.78 ± 0.30^{a}	74.09 ± 0.03^{b}	59.64 ± 0.06^{e}
Pro	106.92 ± 0.06^{e}	117.74 ± 0.05^{b}	113.76 ± 0.10^{d}	121.74 ± 0.50^{a}	115.33 ± 0.05^{c}	97.05 ± 0.19^{f}

Note: Data are mean ± SD. $n = 3$. Different superscript letters within a row indicate significant differences ($p < 0.05$).

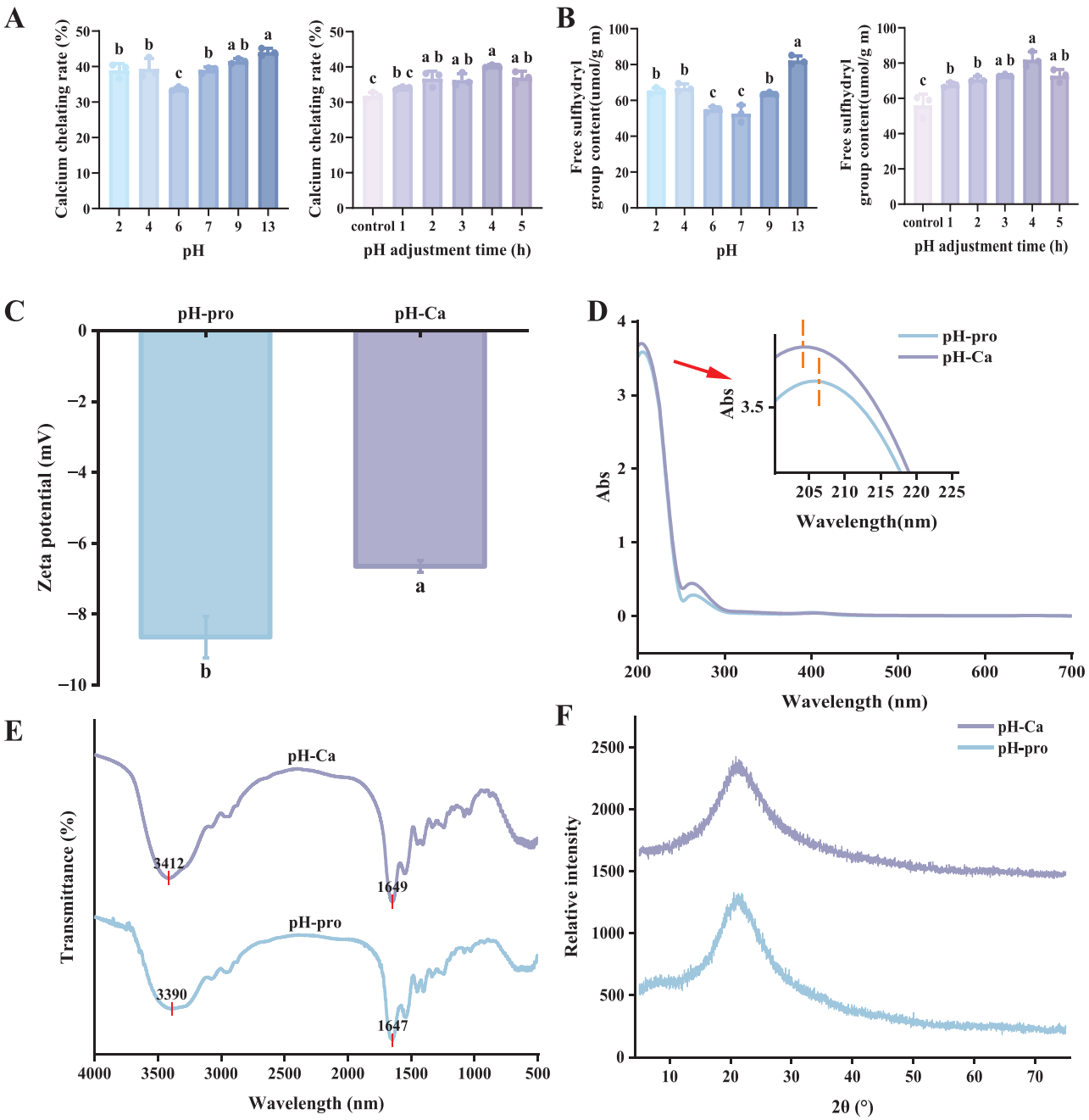

FIGURE 1 | Effects of pH-shift treatment on calcium chelation behavior and structural features of *Chlorella pyrenoidosa* protein/peptide–calcium complexes: (A) calcium chelation rate under different pH conditions and treatment times; (B) free sulfhydryl (–SH) content; (C) zeta potential of pH-treated protein (pH-pro) and peptide–calcium complexes (pH–Ca); (D) UV–Vis spectra (200–700 nm); (E) FTIR spectra (4000–500 cm^{-1}); and (F) XRD patterns ($2\theta = 5°–75°$). Data are presented as mean ± SD ($n = 3$). Different letters indicate significant differences among groups ($p < 0.05$).

metabolic cage study. Compared with the $CaCO_3$ and native-pro-Ca groups, rats receiving pH–Ca supplementation exhibited a significantly higher AAR (Figure 2A). Consistently, fecal Ca excretion was significantly reduced in the pH–Ca group (Figure 2B).

In addition, net Ca retention was markedly increased in rats supplemented with pH–Ca relative to the $CaCO_3$ and Native-pro-Ca groups (Figure 2C). Together, these results indicate that pH–Ca supplementation improves Ca absorption efficiency and reduces intestinal Ca loss, leading to enhanced Ca retention in vivo. The detailed quantitative indices of calcium balance for each group are presented in Table S4.

3.4 | Bone Growth, Mineralization, and Microstructural Properties

Femur and tibia length, DW index, and bone Ca content were significantly reduced in the model group and were more effectively restored by pH–Ca than by $CaCO_3$ or native-pro-Ca (Figure 2D–F). Mechanical testing further showed that fracture force, work

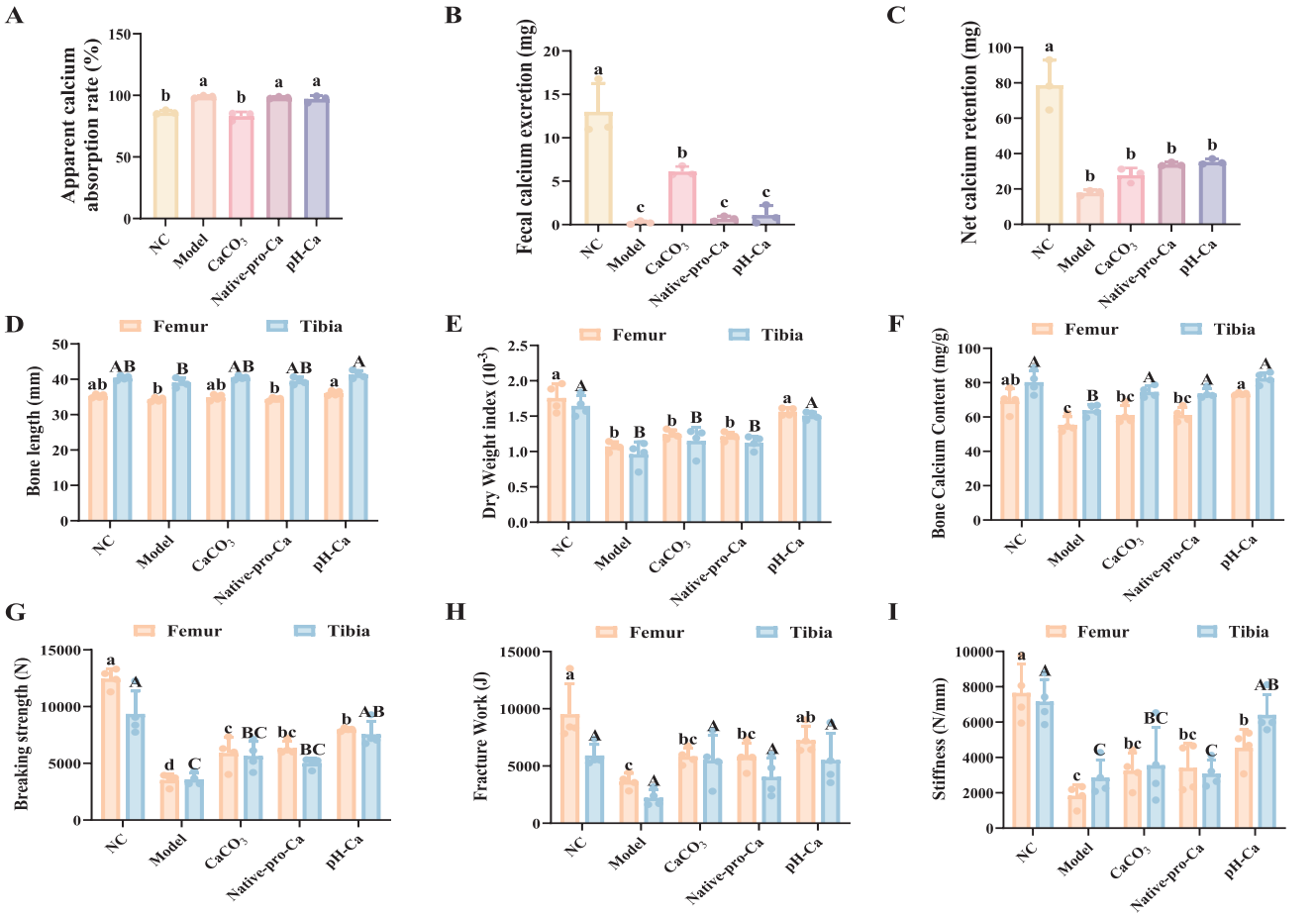

FIGURE 2 | Effects of different calcium sources supplementation on calcium metabolism, bone growth indices, and mechanical properties in calcium-deficient rats: (A) apparent calcium absorption (AAR); (B) fecal calcium excretion; (C) net calcium retention; (D) bone length; (E) dry weight (DW) index; (F) bone calcium content; (G) fracture force; (H) work of fracture; and (I) stiffness determined by three-point bending tests. Data are presented as mean ± SD ($n = 4$). Different letters indicate significant differences among groups ($p < 0.05$).

TABLE 3 | Free carboxyl group content of indicated pH.

Sample	Q_{COOH} (mmol/g)
pH 2	85.75 ± 0.20^{c}
pH 4	86.31 ± 0.16^{c}
pH 6	63.17 ± 0.31^{e}
pH 7	77.86 ± 0.48^{d}
pH 9	87.74 ± 0.06^{b}
pH 13	90.21 ± 0.31^{a}

Note: All data are presented as ± SD $n = 3$. Different superscript letters within the same row denote statistically significant differences between experimental groups at the level of $p < 0.05$.

of fracture, and stiffness were significantly enhanced in the pH–Ca group compared with the model group (Figure 2G–I), whereas $CaCO_3$ and Native-pro-Ca showed limited or partial improvement.

Micro-CT analysis revealed sparse and disorganized trabecular bone and reduced cortical thickness in Ca-deficient rats (Figure 3A). These structural deficits were partially improved by $CaCO_3$ and Native-pro-Ca, whereas pH–Ca supplementation produced denser trabecular architecture, improved connectivity, and increased cortical thickness, as confirmed by quantitative microarchitectural parameters (Figure 3B). Histological evaluation further supported these findings. OCN immunohistochemistry showed reduced osteoblast-associated staining in Ca-deficient rats, which was restored following supplementation, with pH–Ca producing staining intensity and distribution approaching that of the NC (Figure 3C). Conversely, TRAP staining revealed elevated osteoclast density in the model group, which was only partially reduced by $CaCO_3$ and native-pro-Ca, while pH–Ca reduced TRAP-positive cell numbers to levels comparable with the NC (Figure 3D).

3.5 | Serum Biochemical Markers of Bone Turnover and Inflammatory Status

No significant differences in body weight gain were observed among groups (Table 5). Serum Ca and phosphorus levels remained comparable across treatments (Figure 4A,B). The normal serum Ca level in the model group, alongside the decrease observed in some Ca intervention groups, especially the $CaCO_3$ group, may result from the precise regulation of Ca homeostasis

TABLE 4 | Comparison of protein/peptide–calcium complexes reported in the literature and the present study.

Source	Hydrolysis method	Best calcium-binding performance	Bioavailability evidence	References
Whey protein	Flavourzyme, protamex	67.81 μg/mg, ~20% higher than $CaCl_2$	~20% higher calcium retention at pH 8	S. L. Huang et al. (2015)
Casein	Trypsin	23.37%	MC3T3-E1 proliferation increased by ~22%–28%	W. Huang et al. (2022)
Soybean protein	Trypsin	345 μg/mg, ~25% higher than control	Intracellular Ca^{2+} increased by ~30 nM in Caco-2 cells	Lee et al. (2005)
Moringa oleifera leaf	Alkaline protease	83.61%	Ca transport increased by ~30 μg/well, improved bone microstructure	Men et al. (2025)
Tilapia bone collagen	Neutral protease	18.80–35.73 mg/g	Ca transport increased by ~89%–202% in Caco-2 monolayers	Liao et al. (2020)
Alaska pollock	Pepsin, α-chymotrypsin, trypsin	125.36 mM Ca^{2+}/g	Ca transport >4-fold higher than blank	Eom and Nam (2024)
pH–Ca	pH-shift	44.04%	Increased bone calcium content and strength	This work

Note: The calcium-binding performance and bioavailability evidence were reported using different experimental models and evaluation criteria in each study. The comparison is intended to be qualitative rather than quantitative.

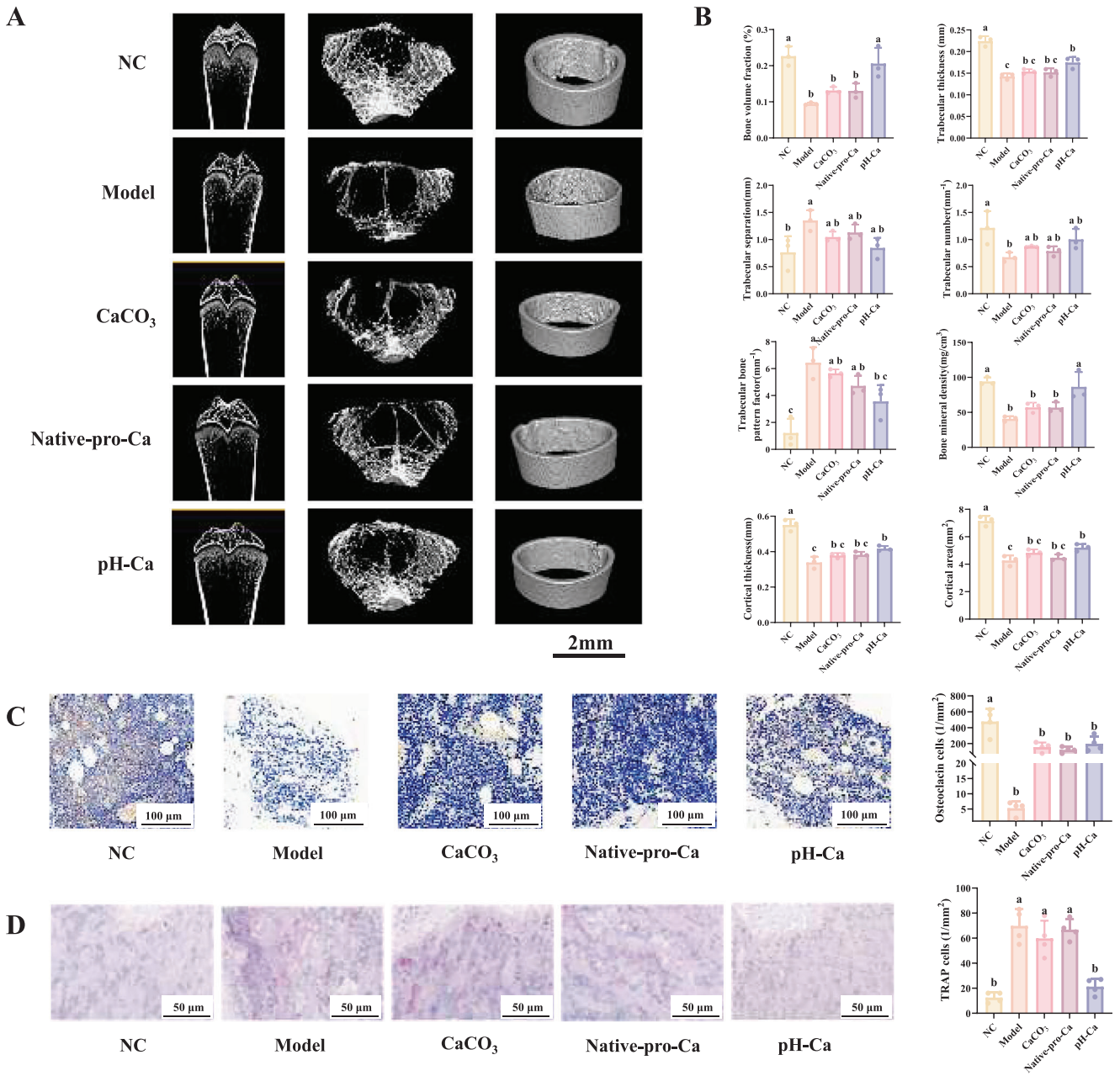

FIGURE 3 | Femoral microarchitecture and histological evaluation of bone formation and resorption: (A) representative three-dimensional micro-CT reconstructions of femoral trabecular bone; (B) quantitative microarchitectural parameters, including BV/TV, Tb.Th, Tb.Sp, Tb.N, Tb.Pf, BMD, Ct.Th, and Ct.Ar; (C) representative osteocalcin (OCN) immunohistochemical staining and quantification of OCN-positive cells; and (D) representative TRAP staining and quantification of TRAP-positive osteoclasts. Scale bars: 100 μm for OCN staining and 50 μm for TRAP staining. Data are presented as mean ± SD ($n = 3$). Different letters indicate significant differences among groups ($p < 0.05$).

in the body, as well as the timing of blood sampling and the characteristics of total Ca measurement. This can be jointly assessed through ALP and PTH levels (Figure 4C,D). In contrast, Ca deficiency significantly elevated ALP and PTH levels, whereas supplementation attenuated these changes, with pH–Ca restoring values closest to the NC. When the body is in a state of insufficient Ca intake that disrupts Ca homeostasis, ALP levels markedly increase (Naylor and Eastell 2012; L. Wang et al. 2012), and PTH is rapidly secreted, prompting rapid skeletal Ca mobilization to regulate serum Ca dynamics (N. Zhao, Hu, et al. 2014). Therefore, the serum Ca level in the model group did not show significant differences. After Ca intervention, the decreases in ALP and PTH levels indicate that the compensatory regulatory axis was partly corrected (G. Liu et al. 2021). The model demonstrates secondary hyperparathyroidism accompanied by hypophosphatemia, which is likely due to the phosphaturic effect of PTH. PTH inhibits renal phosphate reabsorption to maintain the Ca-phosphorus product during periods of high bone resorption. Bone formation markers (OCN and PINP) were reduced, and resorption markers (TRAP-5b and CTX-I) were elevated in the model group; these alterations were most effectively normalized by pH–Ca supplementation (Figure 4E–H). Pro-inflammatory cytokines, including IL-6, IL-17, and TNF-α, were also markedly increased under Ca deficiency and were reduced following supplementation, with the greatest

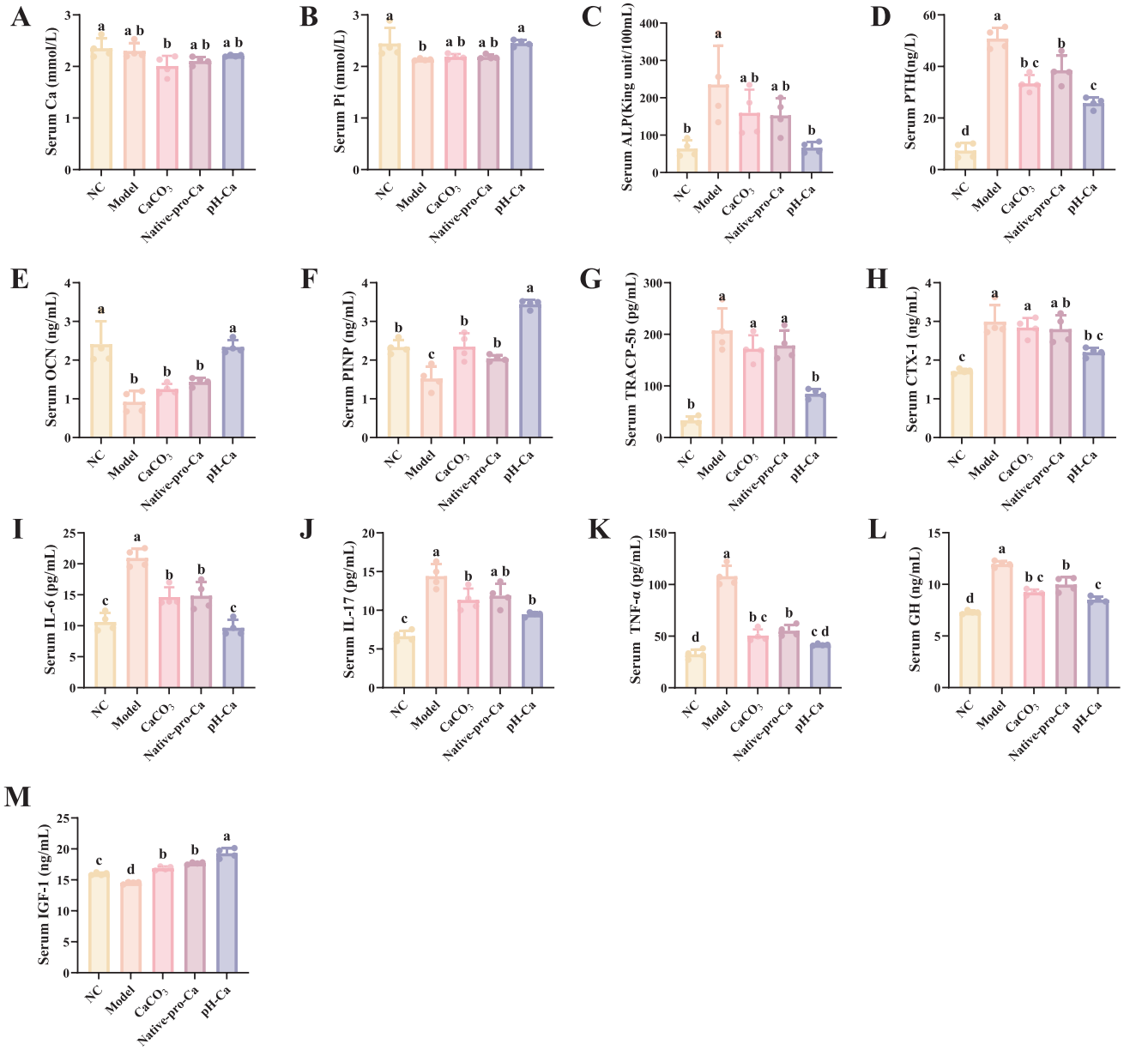

FIGURE 4 | Serum biochemical parameters and inflammatory cytokines in calcium-deficient rats administered different calcium sources: (A) serum calcium (Ca); (B) serum phosphorus (P); (C) alkaline phosphatase (ALP); (D) parathyroid hormone (PTH); (E) osteocalcin (OCN); (F) N-terminal propeptide of Type I procollagen (PINP); (G) tartrate-resistant acid phosphatase 5b (TRAP-5b); (H) C-terminal telopeptide of type I collagen (CTX-I); (I) interleukin-6 (IL-6); (J) interleukin-17 (IL-17); (K) tumor necrosis factor-α (TNF-α); (L) growth hormone (GH); and (M) insulin-like growth factor 1 (IGF-1). Data are presented as mean ± SD ($n = 4$). Different letters indicate significant differences among groups ($p < 0.05$).

reduction observed in the pH–Ca group (Figure 4I–K). As shown in Figure 4L,M, compared with the NC group, the model group exhibited a typical dysregulated state: Serum GH levels were abnormally elevated, whereas serum insulin-like growth factor 1 (IGF-1) levels were significantly reduced. After supplementation with different Ca agents, all intervention groups partially corrected this dysregulation. Among them, the pH–Ca group demonstrated the most pronounced regulatory effect: It not only effectively reduced the elevated serum GH levels (comparable to $CaCO_3$ and native-pro-Ca) but also restored serum IGF-1 to the highest level, showing no statistically significant difference from the NC group, and performed significantly better than the other two Ca supplements. This indicates that pH–Ca, through its optimized bioavailability, most effectively restores systemic Ca homeostasis, thereby repairing the impaired signaling of the GH/IGF-1 axis.

3.6 | Duodenal Morphology and Ca Transport-Related Gene Expression

Shortened villi and disrupted mucosal architecture were observed in the model group (Figure 5A–E). Figure 5E clearly shows that the crypt depth in the Ca-deficient model group was significantly

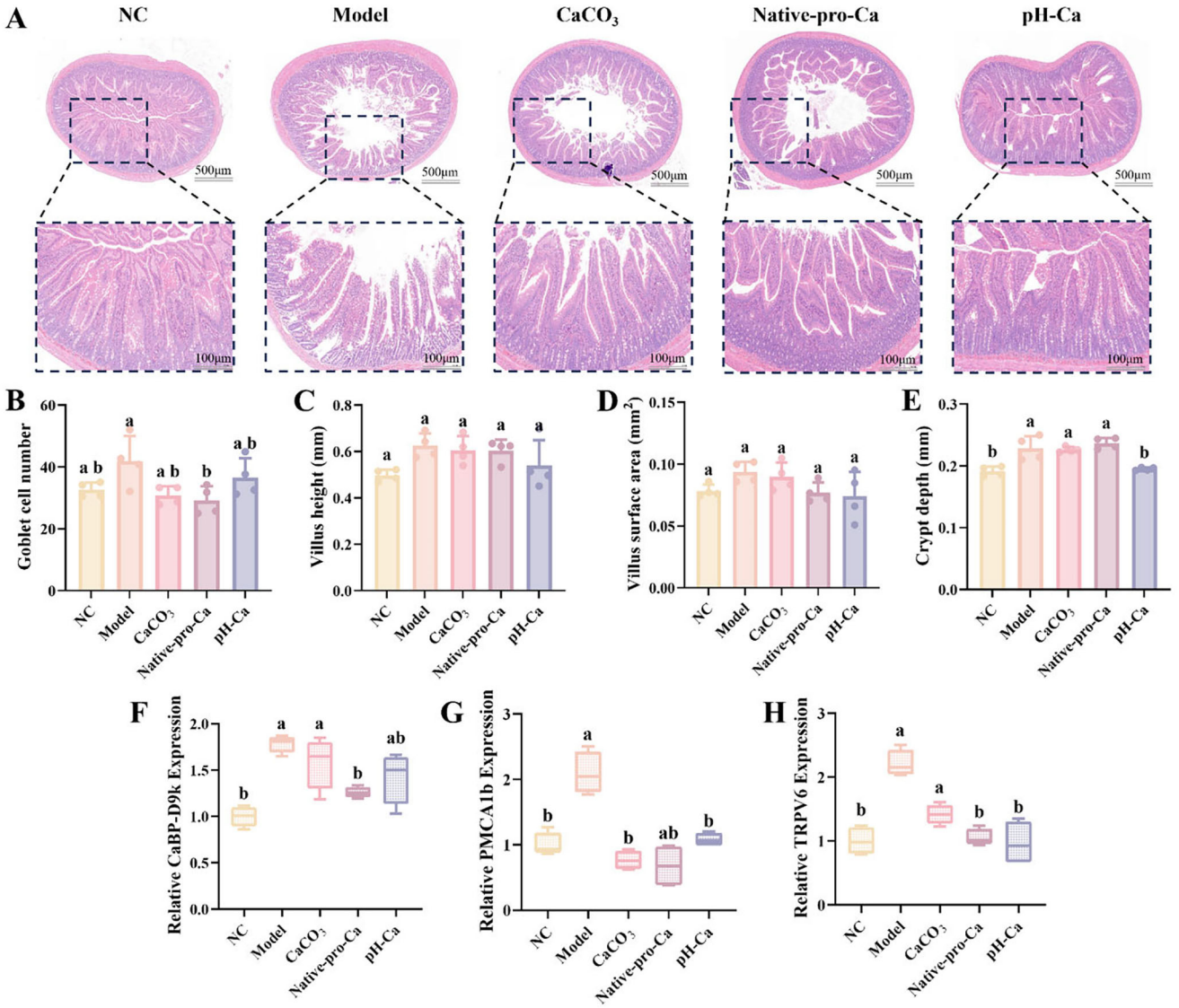

FIGURE 5 | Duodenal morphology, histomorphometric analysis, and relative mRNA expression of calcium transport-related genes: (A) representative H&E-stained sections (scale bar as indicated); (B) goblet cell counts; (C) villus height; (D) villus area; (E) crypt depth; (F) Relative mRNA expression of *CaBP-D9k*; (G) *PMCA1b*; and (H) *TRPV6* in duodenal tissue. Data are expressed as mean ± SD ($n = 4$ for histomorphometric analysis, $n = 4$ for mRNA expression). Different letters indicate significant differences among groups ($p < 0.05$).

higher than that in the NC group. This reflects a compensatory structural remodeling of the intestinal mucosa in response to Ca deficiency. After Ca intervention, the crypt depth decreased in all three intervention groups. Specifically, the pH–Ca group showed a significant reduction compared to the model group, returning to a level comparable to the NC group. Crypt depth reflects the rate of intestinal epithelial cell formation. Shallower crypts indicate accelerated maturation of enterocytes and enhanced absorptive function, whereas deeper crypts suggest increased tissue metabolism and elevated nutritional demand in the organism (K. Yamauchi et al. 1995, 1996). Supplementation partially restored these features, with pH–Ca producing villus height and goblet cell parameters comparable to the NC. Consistent with these changes, expression of *TRPV6*, *CaBP-D9k*, and *PMCA1b* was significantly elevated in Ca-deficient rats (Figure 5F–H). pH–Ca supplementation attenuated this transcriptional response, yielding expression levels closer to those of the NC, whereas $CaCO_3$ and Native-pro-Ca showed intermediate effects.

3.7 | Gut Microbiota Diversity and Compositional Modulation

α-Diversity indices (Chao1, ACE, observed_ASV, PD_whole_tree) were significantly reduced in the Model group and increased following pH–Ca supplementation (Figure 6A). OPLS-DA analysis showed clear separation between microbial communities in the pH–Ca and $CaCO_3$ groups (Figure 6B). At the genus level, pH–Ca increased the relative abundance of *Lactobacillus* and decreased *Allobaculum* compared with the Model group (Figure 6C,D). LEfSe analysis further identified enrichment of Muribaculaceae in the pH–Ca group, whereas taxa associated with dysbiosis,

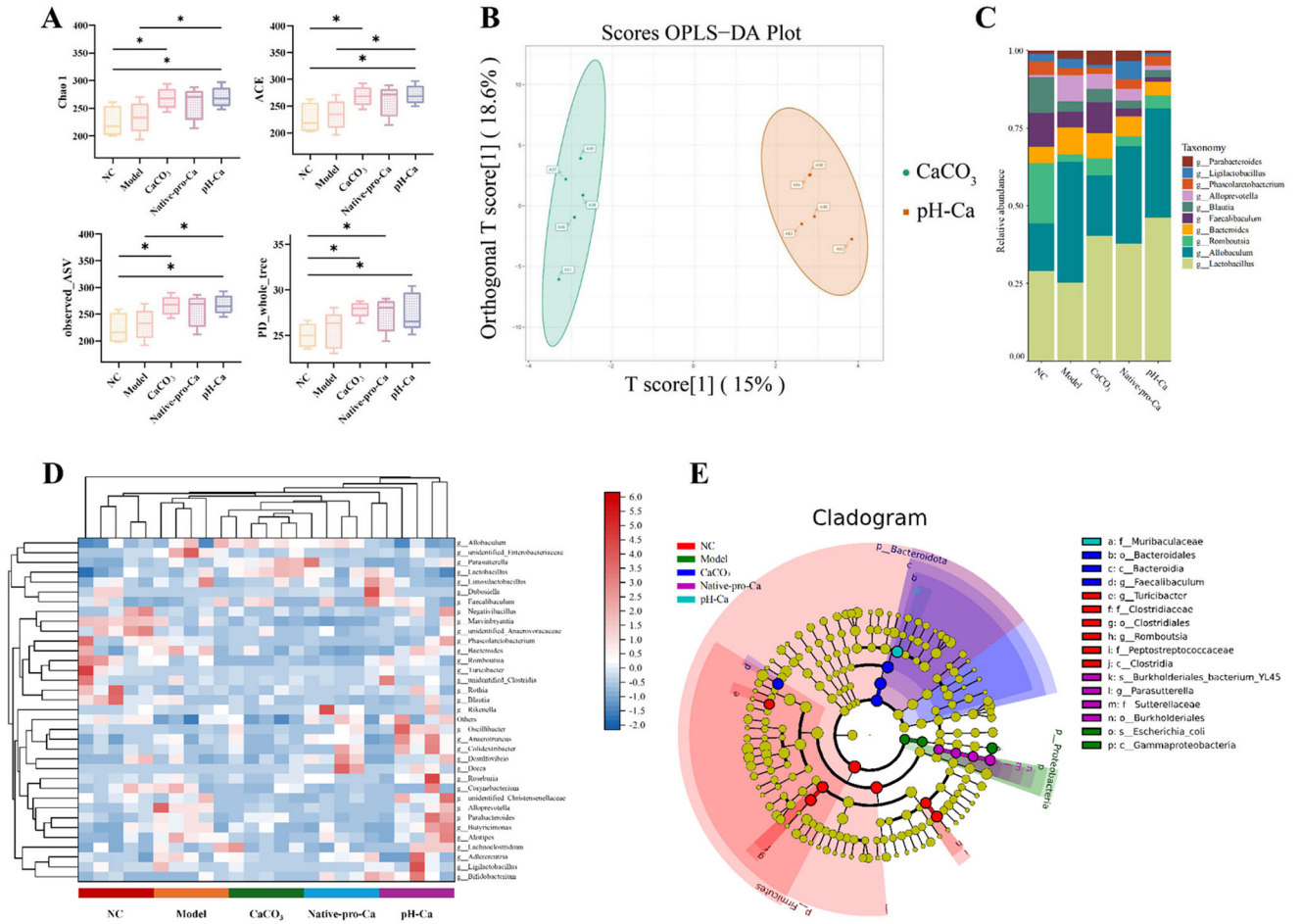

FIGURE 6 | Gut microbiota diversity and compositional changes in calcium-deficient rats supplemented with different calcium sources: (A) alpha-diversity indices; (B) OPLS-DA score plot comparing the pH–Ca and $CaCO_3$ groups; (C) relative abundance of microbial taxa at the phylum level; (D) heatmap of genus-level microbial composition; and (E) cladogram from LEfSe analysis highlighting differentially enriched taxa. Data are presented as mean ± SD where applicable ($n = 5$). Differential taxa were identified using the Kruskal–Wallis test ($p < 0.05$).

including *Escherichia coli*, were enriched in Ca-deficient rats (Figure 6E).

4 | Discussion

pH-shift technology is widely applied to modulate the conformation and surface chemistry of plant-based proteins (Tang et al. 2023), and systematic reviews have demonstrated its pronounced effects on protein structure and functionality (Long et al. 2025; Sultan et al. 2024). In the present study, Ca chelation increased progressively with alkalinity and reached a maximum at pH 13 (Figure 1A), consistent with extensive protein unfolding and enhanced exposure of Ca-binding sites under strong alkaline conditions (Dudev and Lim 2003). Mechanistically, deprotonation of carboxyl groups at high pH increases negative charge density, thereby strengthening electrostatic attraction and coordination with Ca^{2+} (Jiang et al. 2011). Compared with protease-dependent strategies, the enzyme-free pH-shift approach simplifies processing and avoids cost and batch-to-batch variability associated with enzymatic hydrolysis and fractionation (Fan et al. 2024; Martoccia et al. 2025). The gradual increase in chelation under acidic conditions (pH 2–4) likely reflects partial unfolding and exposure of buried coordination groups, whereas reduced chelation near neutral pH may result from partial refolding and re-burial of these sites (Figure 1A). Although pH 13 was optimal in this study, industrial application should consider alkali consumption, neutralization salt burden, and potential alkaline side reactions (Du et al. 2025), motivating future optimization toward milder but intensified conditions. Enzymatic hydrolysis is the most commonly employed strategy for generating peptide–Ca complexes with high Ca-binding capacity (Erdem and Woodley 2024; M. Liu et al. 2025). However, it is often associated with higher cost, longer processing time, and limited scalability. As summarized in Table 4, the Ca-binding performance of pH–Ca prepared via the pH-shift approach, although lower than that reported for some enzymatically derived peptide–Ca complexes, reached a substantial proportion of the chelation levels achieved by enzymatic methods. Notably, a chelation rate of 44.04% obtained without enzymatic hydrolysis falls within the lower-to-middle range of values reported for enzyme-based systems. This indicates that pH-shift treatment alone is sufficient to generate protein-derived Ca-binding structures with appreciable chelation efficiency.

Consistent with protein structure unfolding, pH-shift treatment markedly increased free sulfhydryl (–SH) content, particularly under alkaline conditions (Figure 1B). This reflects breakage or rearrangement of disulfide bonds and exposure of previously

TABLE 5 | Body weight gain and organ index of rats.

Group	NC	Model	$CaCO_3$	Native-pro-Ca	pH–Ca
Initial body weight (g)	108.40 ± 4.49[a]	110.07 ± 2.60[a]	109.86 ± 5.07[a]	105.35 ± 5.16[a]	103.86 ± 3.65[a]
Final body weight (g)	364.64 ± 8.80[a]	374.93 ± 13.39[a]	366.76 ± 15.07[a]	366.81 ± 15.01[a]	357.86 ± 7.15[a]
Body weight gain (g)	256.24 ± 8.49[a]	260.29 ± 6.87[a]	256.90 ± 10.18[a]	254.00 ± 6.61[a]	261.46 ± 11.55[a]
Liver weight (g)	9.86 ± 0.74[a]	11.13 ± 0.66[a]	10.52 ± 0.86[a]	10.86 ± 0.73[a]	10.32 ± 1.05[a]
Spleen weight (g)	0.72 ± 0.09[a]	0.73 ± 0.03[a]	0.69 ± 0.06[a]	0.70 ± 0.07[a]	0.68 ± 0.10[a]
Kidney weight (g)	2.56 ± 0.16[a]	3.10 ± 0.35[a]	2.90 ± 0.26[a]	2.81 ± 0.23[a]	2.80 ± 0.21[a]

Note: Data are mean ± SD. $n = 4$. Identical superscript letters within a column indicate no significant differences ($p > 0.05$).
Abbreviation: NC, normal control.

hidden thiol groups (C. Chen et al. 2024; W. Wang et al. 2026). The subsequent decline in –SH content with prolonged treatment likely stems from thiol oxidation and disulfide reformation (Jiang et al. 2011), indicating that chelation efficiency depends on balancing exposure of Ca-binding sites with secondary reactions. Although –SH groups are not main Ca-binding ligands, they act as sensitive markers of protein unfolding. Regions exposed through disulfide rearrangement often overlap with carboxylate and backbone carbonyl donors, boosting the density of Ca-coordinating sites.

Amino acid profiling across pH conditions offered supportive but non-definitive insights into chelation behavior (Figure 1A, Table 2). Asp and Glu contents increased under acidic to near-neutral conditions, whereas their notable decrease at pH 13 aligned with maximal chelation efficiency. This pattern may stem from enhanced binding efficiency per site of oxygen donors at high pH, driven by extensive deprotonation (X. Zhang et al. 2021), as well as alkali-driven protein chain shortening that boosts terminal donor density (Jian et al. 2025). In addition, alkaline deamidation and transient succinimide formation can interfere with amino acid quantification, resulting in underestimation of Asp and Glu after hydrolysis (Cao et al. 2019). Thus, bulk composition alone may underestimate the functional donor capacity under extreme alkaline conditions.

Carboxyl groups ($-COO^-$), particularly those from Asp/Glu side chains, are among the most common oxygen ligands coordinating Ca^{2+} in protein Ca-binding sites (Bu et al. 2024). In the present study, the significantly increased free carboxyl group content (Q_{COOH}) at pH 13 suggests that strong alkaline pH-shift treatment promoted the exposure of carboxyl ligands, which could contribute to the enhanced Ca chelation observed under the same condition. Importantly, Q_{COOH} should be interpreted as an indirect indicator of potential ligand availability rather than a direct measurement of Ca^{2+} coordination geometry or binding stoichiometry. Therefore, the maximal chelation at pH 13 likely reflects effects of ligand exposure of binding domains, rather than carboxyl content alone.

Multiple orthogonal techniques collectively confirmed the formation of a coordinated protein/peptide–Ca complex following pH-shift treatment (Figure 1C–F). Lower absolute zeta potential after chelation indicates charge shielding and ion-bridging effects linked to Ca^{2+} coordination, not enhanced electrostatic stabilization (S. L. Huang et al. 2015; Qu et al. 2022). A hypochromic shift in UV–Vis spectra and characteristic FTIR band shifts point to changes in chromophore environments and involvement of backbone carbonyl and carboxylate groups in Ca binding (Bao et al. 2021; Ding et al. 2025; Qu et al. 2022; Wu et al. 2019). Broad XRD patterns additionally support a mostly amorphous complex with low crystallinity, ruling out formation of crystalline inorganic Ca salts. Traditional calcium supplements (e.g., $CaCO_3$) readily interact with other endogenous components in vivo (e.g., phosphates and oxalates) to form insoluble precipitates that are poorly absorbed and readily excreted (R. Liang et al. 2016; Suehiro et al. 2019). Such precipitates not only result in the ineffective loss of calcium sources but also may promote the formation of calculi (Jahnen-Dechent et al. 2011), and even cause damage to the intestinal tract. Furthermore, in cases of insufficient gastric acidity or accelerated gastric emptying in the body, the inadequate

dissolution of calcium carbonate will directly reduce the content of bioavailable calcium for the host. In contrast, the CPP/peptide–calcium complexes prepared via the pH-shift method can promote the full exposure of active sites, including carboxyl groups (–COOH) and sulfhydryl groups (–SH) in protein/peptide chains that are capable of coordinating with Ca^{2+} through pH-shift treatment. The resulting calcium-peptide chelates exhibit excellent stability in the gastrointestinal environment (Lin et al. 2024) and can effectively circumvent the aforementioned application limitations of traditional calcium carbonate. This amorphous, colloidally reorganized protein/peptide–Ca complex may retain higher Ca solubility during gastrointestinal transit and minimize precipitation compared to $CaCO_3$.

A five-fold RDI calcium dosage was used in this study according to previous reports to avoid insufficient calcium as a confounding factor and to magnify differences among calcium sources in a calcium-deficient model (Y. Liang et al. 2025). However, this supraphysiological dose may saturate active calcium absorption, leading to dominant passive diffusion that could mask subtle differences in bioavailability (Lieben et al. 2010). In addition, the high dosage may limit direct clinical relevance. Future studies with physiological calcium intake are warranted to verify our findings.

Efficient Ca supplementation depends not only on Ca intake but also on intestinal absorption, reduced excretion, and effective retention (Wheeler et al. 2020). In the present study, the Ca metabolism experiment provided integrated physiological evidence supporting the improved utilization of pH–Ca in vivo. Compared with $CaCO_3$ and native-pro-Ca, pH–Ca supplementation significantly enhanced apparent Ca absorption while simultaneously reducing fecal Ca excretion, resulting in increased net Ca retention. These coordinated changes suggest that Ca bound to pH–Ca is more readily released and absorbed in the gastrointestinal tract and is less susceptible to precipitation or loss during intestinal transit (H. Liu et al. 2017). The improved retention efficiency indicates that a greater proportion of absorbed Ca is available for subsequent physiological utilization (Veldurthy et al. 2016). Importantly, this enhanced Ca utilization efficiency offers a mechanistic explanation for the superior effects of pH–Ca on bone Ca deposition and bone strength observed in this study.

It should first be noted that the findings of this study are primarily applicable to growing skeletons during development, and the conclusions should not be directly extrapolated to adults, especially to bone metabolism in adulthood or postmenopause, which is significantly regulated by sex hormones (Weitzmann and Pacifici 2006). These structural and colloidal features translated into clear physiological benefits in Ca-deficient rats. pH–Ca supplementation more effectively restored bone mass indices and mechanical strength than $CaCO_3$ or untreated protein–Ca complexes (Figure 2). At the microstructural scale, micro-CT analysis revealed denser trabecular architecture and increased cortical thickness in the pH–Ca group (Figure 3A,B). Histological analyses further showed increased OCN-positive osteoblasts and reduced TRAP-positive osteoclasts (Figure 3C,D), indicating a shift toward bone formation and reduced resorption. These findings are consistent with the functional advantage of coordinated Ca forms with lower precipitation propensity may help support sustained Ca availability for bone remodeling (Hua et al. 2019).

Future systematic comparisons in female animals, as well as studies on adult/postmenopausal bone health, will be essential directions for verifying the clinical extrapolation of the findings from this study. Moreover, the assessment of long-term bone homeostasis and bone remodeling in adulthood still requires longer term studies or alternative animal models for validation. Nevertheless, the present findings should be interpreted within the context of a growing male rat model. Further studies are warranted to systematically evaluate pH–Ca in female animals and in adult and postmenopausal-relevant models, where bone metabolism is strongly influenced by sex hormones.

Ca deficiency also disrupted systemic bone turnover and inflammatory status, as reflected by elevated PTH, ALP, GH, and pro-inflammatory cytokines (Figure 4). pH–Ca supplementation more effectively normalized these markers than $CaCO_3$, reducing IL-6, IL-17, and TNF-α levels. This is biologically relevant because osteo-immune mediators can promote osteoclastogenesis and exacerbate bone loss (Aurora and Silva 2023; Kim et al. 2015). In the present study, calcium deficiency–induced intestinal/systemic chronic low-grade inflammation may be a key contributor to impairment of the GH/IGF-1 axis. IL-6, TNF-α, and IL-17 were significantly elevated in the model group, and these pro-inflammatory cytokines can suppress hepatic GH receptor (GHR) expression, thereby triggering systemic GH resistance (Yuen et al. 2024; Y. Zhao, Xiao, et al. 2014). Once GH sensitivity declines, hepatic IGF-1 synthesis and secretion become insufficient, weakening GH-mediated bone growth and consequently impairing growth plate chondrocyte proliferation/differentiation and bone mineralization (Dixit et al. 2021). pH–Ca may reduce the release of inflammatory cytokines by improving calcium homeostasis, alleviate GH resistance, and restore hepatic IGF-1 production, thereby re-establishing GH/IGF-1-dependent regulation of the growth plate and bone formation. Although this study measured systemic serum biomarkers and did not directly assess local IGF-1 levels in the growth plate or downstream signaling pathways such as RANKL/OPG balance and NF-κB activation were not directly examined, the coordinated improvement in serum markers, histological indices, and bone microarchitecture points to a systemic environment less conducive to excessive bone resorption (Roodman 1993; Terkawi et al. 2022).

At the intestinal level, Ca deficiency impaired duodenal morphology and induced compensatory upregulation of transcellular Ca transport genes (Figure 5). pH–Ca supplementation partially restored villus architecture and goblet cell indices, suggesting improved mucosal conditions for nutrient handling. Meanwhile, normalization of *TRPV6*, *CaBP-D9k*, and *PMCA1b* expression toward control levels should be interpreted as reduced compensatory demand rather than diminished absorption capacity. Under low-Ca intake, upregulation of these transporters reflects an adaptive response to limited luminal Ca. Thus, attenuation of this response in the pH–Ca group likely reflects improved luminal Ca availability and reduced precipitation, even though direct Ca absorption was not measured (Raveschot et al. 2020).

Finally, pH–Ca supplementation partially restored gut microbiota diversity and reshaped community composition under Ca-deficient feeding (Figure 6). Enrichment of *Lactobacillus* and Muribaculaceae, alongside reduced abundance of potentially

dysbiotic taxa such as *E. coli*, aligns with emerging evidence that gut microbiota can influence mineral utilization through modulation of barrier function and intestinal microenvironment (Raveschot et al. 2020; Varvara and Vodnar 2024). Muribaculaceae, in particular, has been associated with polysaccharide utilization and SCFA-linked metabolic contexts in rodent models (Hadadi et al. 2021; Zhu et al. 2020). Nevertheless, 16S rRNA profiling provides associative rather than causal insight. Future studies integrating functional readouts such as SCFA production, targeted metabolomics, and Ca balance assays will be required to clarify the contribution of microbiota-mediated pathways to the enhanced efficacy of pH–Ca. Future studies should focus on dose-response relationships, direct quantification of Ca availability and retention, and clarification of downstream signaling pathways linking Ca delivery to bone remodeling and host-microbiota interactions.

5 | Conclusion

In summary, a single-step enzyme-free pH-shift strategy was successfully used to produce CPP–Ca complexes with distinct coordination and colloidal properties. Spectroscopic and diffraction analyses confirmed the formation of a predominantly amorphous protein/peptide–Ca complex driven by Ca coordination with carboxylate and backbone functional groups. Compared with $CaCO_3$ and untreated protein–Ca complexes, pH–Ca consistently showed superior biological performance. In Ca-deficient rats, the complexes improved bone microarchitecture and strength and were accompanied by favorable intestinal morphology and Ca transport-related responses. Beyond skeletal outcomes, pH–Ca supplementation was associated with improved intestinal morphology and supportive modulation of gut microbiota composition, including increased *Lactobacillus* and enrichment of Muribaculaceae, whereas taxa associated with dysbiosis (e.g., *E. coli*) were reduced. These findings suggest that coordinated peptide–Ca delivery may help create a more favorable intestinal environment for Ca utilization. Collectively, this study underscores that Ca coordination chemistry and colloidal form, not just Ca dose, are key to biological efficacy. The enzyme-free pH-shift approach provides a clean-label, scalable alternative to protease-dependent processes and offers a practical framework for designing food-grade Ca delivery systems. Future studies should focus on dose-response relationships, direct quantification of Ca availability and retention, and clarification of downstream signaling pathways linking Ca delivery to bone remodeling and host-microbiota interactions.

Author Contributions

Yan Yang: conceptualization, methodology, data curation, formal analysis, writing – original draft, writing – review and editing. **Shenwan Wang**: conceptualization, methodology, investigation, data curation, writing – original draft, writing – review and editing. **Qimeng Zhou**: methodology, software, formal analysis. **Ye Qi**: investigation, data curation, formal analysis. **Bin Zhou**: resources, data curation, software. **Jing Li**: investigation, data curation, supervision, project administration. **Tao Hou**: conceptualization, supervision. **Bin Li**: investigation, resources, supervision. **Hongshan Liang**: supervision, writing – review and editing, project administration, funding acquisition.

Acknowledgments

This work was financially supported by National Key R&D Program of China (2023YFF1104304) and the Fundamental Research Funds for the Central Universities (Project No:2662025SPPY004).

Conflicts of Interest

The authors declare no conflicts of interest.

Data Availability Statement

The data that support the findings of this study are available from the corresponding author upon reasonable request.

References

Aurora, R., and M. J. Silva. 2023. "T Cells Heal Bone Fractures With Help From the Gut Microbiome." *Journal of Clinical Investigation* 133, no. 8: e167311. https://doi.org/10.1172/jci167311.

Bao, Z., P. Zhang, N. Sun, and S. Lin. 2021. "Elucidating the Calcium-Binding Site, Absorption Activities, and Thermal Stability of Egg White Peptide–Calcium Chelate." *Foods* 10, no. 11: 2565. https://doi.org/10.3390/foods10112565.

Bu, G., X. Zhao, M. Wang, et al. 2024. "Identification of Calcium Chelating Peptides From Peanut Protein Hydrolysate and Absorption Activity of Peptide-Calcium Complex." *Journal of the Science of Food and Agriculture* 104, no. 11: 6676–6686. https://doi.org/10.1002/jsfa.13493.

Cao, M., W. Xu, B. Niu, et al. 2019. "An Automated and Qualified Platform Method for Site-Specific Succinimide and Deamidation Quantitation Using Low-pH Peptide Mapping." *Journal of Pharmaceutical Sciences* 108, no. 11: 3540–3549. https://doi.org/10.1016/j.xphs.2019.07.019.

Chen, C., Z. Liu, W. Xiong, Y. Yao, J. Li, and L. Wang. 2024. "Effect of Alkaline Treatment Duration on Rapeseed Protein During pH-Shift Process: Unveiling Physicochemical Properties and Enhanced Emulsifying Performance." *Food Chemistry* 459: 140280. https://doi.org/10.1016/j.foodchem.2024.140280.

Chen, J., X. Qiu, G. Hao, M. Zhang, and W. Weng. 2017. "Preparation and Bioavailability of Calcium-Chelating Peptide Complex From Tilapia Skin Hydrolysates." *Journal of the Science of Food and Agriculture* 97, no. 14: 4898–4903. https://doi.org/10.1002/jsfa.8363.

Chen, Y., J. Chen, C. Chang, et al. 2019. "Physicochemical and Functional Properties of Proteins Extracted From Three Microalgal Species." *Food Hydrocolloids* 96: 510–517. https://doi.org/10.1016/j.foodhyd.2019.05.025.

Ding, Q., A. R. Sheikh, Y. Zhu, et al. 2025. "Preparation and Characterization of Ultrasound-Assisted Novel Peptide–Calcium Chelates From Nannocholoropsis Oceanica." *Food and Bioprocess Technology* 18, no. 3: 2820–2839. https://doi.org/10.1007/s11947-024-03634-3.

Dixit, M., S. B. Poudel, and S. Yakar. 2021. "Effects of GH/IGF Axis on Bone and Cartilage." *Molecular and Cellular Endocrinology* 519: 111052. https://doi.org/10.1016/j.mce.2020.111052.

Du, Y., Q. Tian, X. Kuang, Y. Deng, Y. Jiang, and J. Yi. 2025. "Advanced Application of Alkaline/Basic Electrolyzed Water in the Food and Agriculture Industry as Cleaning, Processing, Preserving, and Functional Agents." *Comprehensive Reviews in Food Science and Food Safety* 24, no. 2: e70129. https://doi.org/10.1111/1541-4337.70129.

Dudev, T., and C. Lim. 2003. "Principles Governing Mg, Ca, and Zn Binding and Selectivity in Proteins." *Chemical Reviews* 103, no. 3: 773–788. https://doi.org/10.1021/cr020467n.

Eom, T., and T. J. Nam. 2024. "Calcium Absorption by Alaska Pollock Surimi Protein Hydrolysate Promotes Osteoblast Differentiation." *Journal of Food Science* 89, no. 4: 2482–2493. https://doi.org/10.1111/1750-3841.16988.

Erdem, E., and J. M. Woodley. 2024. "Using Enzymes for Catalysis Under Industrial Conditions." *ACS Catalysis* 14, no. 24: 18436–18441. https://doi.org/10.1021/acscatal.4c05265.

Fan, G., Y. Li, Q. Ye, et al. 2024. "Animal-Derived Free Hydrolysate in Animal Cell Culture: Current Research and Application Advances." *Journal of Tissue Engineering* 15: 20417314241300388. https://doi.org/10.1177/20417314241300388.

Hadadi, N., V. Berweiler, H. Wang, and M. Trajkovski. 2021. "Intestinal Microbiota as a Route for Micronutrient Bioavailability." *Current Opinion in Endocrine and Metabolic Research* 20: 100285. https://doi.org/10.1016/j.coemr.2021.100285..

Hua, P., Y. Xiong, Z. Yu, B. Liu, and L. Zhao. 2019. "Effect of *Chlorella pyrenoidosa* Protein Hydrolysate-Calcium Chelate on Calcium Absorption Metabolism and Gut Microbiota Composition in Low-Calcium Diet-Fed Rats." *Marine Drugs* 17, no. 6: 138763. https://doi.org/10.1016/j.foodchem.2024.138763.

Huang, S. L., L. N. Zhao, X. Cai, et al. 2015. "Purification and Characterisation of a Glutamic Acid-Containing Peptide With Calcium-Binding Capacity From Whey Protein Hydrolysate." *Journal of Dairy Research* 82, no. 1: 29–35. https://doi.org/10.1017/s0022029914000715.

Huang, W., L. Lao, Y. Deng, et al. 2022. "Preparation, Characterization, and Osteogenic Activity Mechanism of Casein Phosphopeptide-Calcium Chelate." *Frontiers in Nutrition* 9: 960228. https://doi.org/10.3389/fnut.2022.960228.

Jahnen-Dechent, W., A. Heiss, C. Schäfer, and M. Ketteler. 2011. "Fetuin-A Regulation of Calcified Matrix Metabolism." *Circulation Research* 108, no. 12: 1494–1509. https://doi.org/10.1161/CIRCRESAHA.110.234260.

Jian, M., K. Wang, Y. Wang, Y. Cheng, and J. Gan. 2025. "The Negative Electrostatic Potential of the Coordination Between Calcium and Carboxyl/Oxygen Group in Calcium-Peptide Complexes Contributes to Calcium Utilization." *Food Chemistry* 464: 141909. https://doi.org/10.1016/j.foodchem.2024.141909.

Jiang, J., Y. L. Xiong, and J. Chen. 2011. "Role of β-Conglycinin and Glycinin Subunits in the pH-Shifting-Induced Structural and Physicochemical Changes of Soy Protein Isolate." *Journal of Food Science* 76, no. 2: C293–C302. https://doi.org/10.1111/j.1750-3841.2010.02035.x.

Kim, H. R., S. H. Lee, H. Y. Kim, and S. H. Lee. 2015. "SAT0016 TH17 Cytokines Regulate Osteoclastogenesis in Rheumatoid Arthritis." *Annals of the Rheumatic Diseases* 74: 655. https://doi.org/10.1136/annrheumdis-2015-eular.1773.

Lee, S. H., J. I. Yang, S. M. Hong, et al. 2005. "Phosphorylation of Peptides Derived From Isolated Soybean Protein: Effects on Calcium Binding, Solubility and Influx Into Caco-2 Cells." *Biofactors* 23, no. 3: 121–128. https://doi.org/10.1002/biof.5520230301.

Li, J., M. Wu, Y. Wang, K. Li, J. Du, and Y. Bai. 2020. "Effect of pH-Shifting Treatment on Structural and Heat Induced Gel Properties of Peanut Protein Isolate." *Food Chemistry* 325: 126921. https://doi.org/10.1016/j.foodchem.2020.126921.

Liang, R., Y. Jiang, W. Yokoyama, C. Yang, G. Cao, and F. Zhong. 2016. "Preparation of Pickering Emulsions With Short, Medium and Long Chain Triacylglycerols Stabilized by Starch Nanocrystals and Their In Vitro Digestion Properties." *RSC Advances* 6, no. 101: 99496–99508. https://doi.org/10.1039/C6RA18468E.

Liang, Y., Q. Cheng, Z. Chen, and T. Hou. 2025. "Effects of Yeast Protein on the Promotion of Intestinal Calcium Absorption (In Vivo/In Vitro) and Bone Formation (In Vivo) in Rats Fed by Normal and Low-Calcium Diets." *Food Research International* 220: 117179. https://doi.org/10.1016/j.foodres.2025.117179.

Liao, W., H. Chen, W. Jin, Z. Yang, Y. Cao, and J. Miao. 2020. "Three Newly Isolated Calcium-Chelating Peptides From Tilapia Bone Collagen Hydrolysate Enhance Calcium Absorption Activity in Intestinal Caco-2 Cells." *Journal of Agricultural and Food Chemistry* 68, no. 7: 2091–2098. https://doi.org/10.1021/acs.jafc.9b07602.

Lieben, L., B. S. Benn, D. Ajibade, et al. 2010. "Trpv6 Mediates Intestinal Calcium Absorption During Calcium Restriction and Contributes to Bone Homeostasis." *Bone* 47, no. 2: 301–308. https://doi.org/10.1016/j.bone.2010.04.595.

Lin, S., J. Li, X. Hu, et al. 2024. "Potential Dietary Calcium Supplement: Calcium-Chelating Peptides and Peptide-Calcium Complexes Derived From Blue Food Proteins." *Trends in Food Science & Technology* 145: 104364. https://doi.org/10.1016/j.tifs.2024.104364.

Liu, G., B. Guo, S. Sun, et al. 2021. "Promoting the Calcium-Uptake Bioactivity of Casein Phosphopeptides In Vitro and In Vivo." *Frontiers in Nutrition* 8: 743791. https://doi.org/10.3389/fnut.2021.743791.

Liu, H., Y. Lv, J. Xu, and S. Guo. 2017. "Interaction Mode of Calcium-Binding Peptides and Caco-2 Cell Membrane." *Food Research International* 102: 225–233. https://doi.org/10.1016/j.foodres.2017.09.077.

Liu, M., R. Xiao, X. Li, Y. Zhao, and J. Huang. 2025. "A Comprehensive Review of Recombinant Technology in the Food Industry: Exploring Expression Systems, Application, and Future Challenges." *Comprehensive Reviews in Food Science and Food Safety* 24, no. 2: e70078. https://doi.org/10.1111/1541-4337.70078.

Long, R., Y. Huang, M. Dabbour, et al. 2025. "Physical Processing-Assisted pH Shifting for Food Protein Modification: A Comprehensive Review." *Foods* 14: 2360. https://doi.org/10.3390/foods14132360.

Martoccia, M., V. Disca, Y. Jaouhari, M. Bordiga, and J. D. Coïsson. 2025. "Recent Approaches for Bioactive Peptides Production From Pulses and Pseudocereals." *Molecules (Basel, Switzerland)* 30: 4304. https://doi.org/10.3390/molecules30214304.

Men, D., J. Dai, Z. Lei, et al. 2025. "Preparation, Characterization, Stability and Replenishing Calcium Ability of *Moringa oleifera* Leaf Peptide-Calcium Chelates." *Food Research International* 200: 115439. https://doi.org/10.1016/j.foodres.2024.115439.

Mollaev, M., A. Zabolotskii, N. Gorokhovets, et al. 2021. "Expression of Acid Cleavable Asp-Pro Linked Multimeric AFP Peptide in *E. coli*." *Journal of Genetic Engineering and Biotechnology* 19, no. 1: 155. https://doi.org/10.1186/s43141-021-00265-5.

Naylor, K., and R. Eastell. 2012. "Bone Turnover Markers: Use in Osteoporosis." *Nature Reviews Rheumatology* 8, no. 7: 379–389. https://doi.org/10.1038/nrrheum.2012.86.

Pass, C., V. E. MacRae, S. F. Ahmed, and C. Farquharson. 2009. "Inflammatory Cytokines and the GH/IGF-I Axis: Novel Actions on Bone Growth." *Cell Biochemistry and Function* 27, no. 3: 119–127. https://doi.org/10.1002/cbf.1551.

Qu, W., Y. Li, T. Xiong, Y. Feng, H. Ma, and N. Dzidzorgbe Kwaku Akpabli-Tsigbe. 2022. "Calcium-Chelating Improved Zein Peptide Stability, Cellular Uptake, and Bioactivity by Influencing the Structural Characterization." *Food Research International* 162, no. Pt A: 112033. https://doi.org/10.1016/j.foodres.2022.112033.

Raveschot, C., F. Coutte, M. Frémont, et al. 2020. "Probiotic Lactobacillus Strains From Mongolia Improve Calcium Transport and Uptake by Intestinal Cells In Vitro." *Food Research International* 133: 109201. https://doi.org/10.1016/j.foodres.2020.109201.

Roodman, G. D. 1993. "Role of Cytokines in the Regulation of Bone Resorption." *Calcified Tissue International* 53, no. 1: S94–S98. https://doi.org/10.1007/BF01673412.

Suehiro, D., M. Okada, K. Fukami, T. Nakagawa, and T. Hayakawa. 2019. "Maltobionic Acid Enhances Intestinal Absorption of Calcium and Magnesium in Rats." *Bioscience, Biotechnology, and Biochemistry* 83, no. 9: 1766–1773. https://doi.org/10.1080/09168451.2019.1611411.

Sultan, Z., A. Ashfaq, K. Jahan, O. S. Qadri, K. Younis, and O. Yousuf. 2024. "pH Shift Extraction Technique for Plant Proteins: A Promising Technique for Sustainable Development." *Energy Nexus* 16: 100329. https://doi.org/10.1016/j.nexus.2024.100329.

Tang, Y. R., A. K. Stone, Y. Wang, et al. 2023. "Effect of a pH Shift Treatment on the Functional Properties of Individual and Blended Commercial Plant Protein Ingredients." *European Food Research and Technology* 249, no. 8: 1969–1977. https://doi.org/10.1007/s00217-023-04267-0.

Terkawi, M. A., G. Matsumae, T. Shimizu, D. Takahashi, K. Kadoya, and N. Iwasaki. 2022. "Interplay Between Inflammation and Patholog-

ical Bone Resorption: Insights Into Recent Mechanisms and Pathways in Related Diseases for Future Perspectives." *International Journal of Molecular Sciences* 23, no. 3: 1786. https://doi.org/10.3390/ijms23031786.

Ursu, A.-V., A. Marcati, T. Sayd, V. Sante-Lhoutellier, G. Djelveh, and P. Michaud. 2014. "Extraction, Fractionation and Functional Properties of Proteins From the Microalgae *Chlorella vulgaris*." *Bioresource Technology* 157: 134–139. https://doi.org/10.1016/j.biortech.2014.01.071.

Varvara, R.-A., and D. C. Vodnar. 2024. "Probiotic-Driven Advancement: Exploring the Intricacies of Mineral Absorption in the Human Body." *Food Chemistry: X* 21: 101067. https://doi.org/10.1016/j.fochx.2023.101067.

Veldurthy, V., R. Wei, L. Oz, P. Dhawan, Y. H. Jeon, and S. Christakos. 2016. "Vitamin D, Calcium Homeostasis and Aging." *Bone Research* 4: 16041. https://doi.org/10.1038/boneres.2016.41.

Wang, L., S. Chen, R. Liu, and H. Wu. 2012. "A Novel Hydrolytic Product From Flesh of *Mactra veneriformis* and Its Bioactivities in Calcium Supplement." *Journal of Ocean University of China* 11, no. 3: 389–396. https://doi.org/10.1007/s11802-012-1960-4.

Wang, W., X. Li, Z. Fang, and J. Bi. 2026. "Structural Effect of Polygalacturonase Modified Pectin on Polyphenol Enzymatic Oxidation." *Food Hydrocolloids* 172: 112181. https://doi.org/10.1016/j.foodhyd.2025.112181.

Wang,Z., Li,B., and Fang,Y., eds. 2025. *Healthy Food for Children*. Springer.

Weitzmann, M. N. 2006. "Estrogen Deficiency and Bone Loss: An Inflammatory Tale." *Journal of Clinical Investigation* 116, no. 5: 1186–1194. https://doi.org/10.1172/JCI28550.

Wheeler, D. C., B. V. Stefansson, M. Batiushin, et al. 2020. "The Dapagliflozin and Prevention of Adverse Outcomes in Chronic Kidney Disease (DAPA-CKD) Trial: Baseline Characteristics." *Nephrology Dialysis Transplantation* 35, no. 10: 1700–1711. https://doi.org/10.1093/ndt/gfaa234.

Wu, W., L. He, Y. Liang, et al. 2019. "Preparation Process Optimization of Pig Bone Collagen Peptide-Calcium Chelate Using Response Surface Methodology and Its Structural Characterization and Stability Analysis." *Food Chemistry* 284: 80–89. https://doi.org/10.1016/j.foodchem.2019.01.103.

Yamauchi, K., K. Yamamoto, and Y. Isshiki. 1995. "Morphological Alterations of the Intestinal Villi and Absorptive Epithelial Cells in Each Intestinal Part in Fasted Chickens." *Japanese Poultry Science* 32, no. 4: 241–251. https://doi.org/10.2141/jpsa.32.241.

Yamauchi, K., H. Kamisoyama, and Y. Isshiki. 1996. "Effects of Fasting and Refeeding on Structures of the Intestinal Villi and Epithelial Cells in White Leghorn Hens." *British Poultry Science* 37, no. 5: 909–921. https://doi.org/10.1080/00071669608417922.

Yuen, K. C. J., R. Hjortebjerg, A. A. Ganeshalingam, D. R. Clemmons, and J. Frystyk. 2024. "Growth Hormone/Insulin-Like Growth Factor I Axis in Health and Disease States: An Update on the Role of Intra-Portal Insulin." *Frontiers in Endocrinology* 15: 1456195. https://doi.org/10.3389/fendo.2024.1456195.

Zhang, T., Z. Jin, H. Zhao, et al. 2024. "Aqueous Alkaline Phosphate Facilitates the Non-Exchangeable Deuteration of Peptides and Proteins." *RSC Advances* 14, no. 12: 8075–8080. https://doi.org/10.1039/d3ra08636d.

Zhang, X., Q. Jia, M. Li, et al. 2021. "Isolation of a Novel Calcium-Binding Peptide From Phosvitin Hydrolysates and the Study of Its Calcium Chelation Mechanism." *Food Research International* 141: 110169. https://doi.org/10.1016/j.foodres.2021.110169.

Zhao, M., H. He, D. Guo, et al. 2022. "Chitosan Oligosaccharides-Tripolyphosphate Microcapsules as Efficient Vehicles for Desalted Duck Egg White Peptides-Calcium: Fabrication, Entrapment Mechanism and In Vivo Calcium Absorption Studies." *LWT—Food Science and Technology* 154: 112869. https://doi.org/10.1016/j.lwt.2021.112869.

Zhao, N., J. Hu, T. Hou, Z. Ma, C. Wang, and H. He. 2014. "Effects of Desalted Duck Egg White Peptides and Their Products on Calcium Absorption in Rats." *Journal of Functional Foods* 8: 234–242. https://doi.org/10.1016/j.jff.2014.03.022.

Zhao, Y., X. Xiao, S. J. Frank, H. Y. Lin, and Y. Xia. 2014. "Distinct Mechanisms of Induction of Hepatic Growth Hormone Resistance by Endogenous IL-6, TNF-α, and IL-1β." *American Journal of Physiology-Endocrinology and Metabolism* 307, no. 2: E186–E198. https://doi.org/10.1152/ajpendo.00652.2013.

Zhu, L., F. Hua, W. Ding, K. Ding, Y. Zhang, and C. Xu. 2020. "The Correlation Between the Th17/Treg Cell Balance and Bone Health." *Immunity and Ageing* 17: 30. https://doi.org/10.1186/s12979-020-00202-z.

Supporting Information

Additional supporting information can be found online in the Supporting Information section.

Table S1 Serum biochemical marker assay kit information. Table S2 The primer sequences in the research. Table S3 Calcium content of Native-pro-Ca and pH–Ca (mg/g). Table S4 Calcium balance indices.